Small Scale Processes and Entrainment in a Stratocumulus Marine Boundary Layer

David E. Stevens

Atmospheric Sciences Division
Lawrence Livermore National Laboratory
Livermore, California

John B. Bell, Ann S. Almgren,
Vince E. Beckner, and Charles A. Rendleman

Computing Sciences Division
Lawrence Berkeley National Laboratory
Berkeley, California

Abstract

Numerical studies of boundary layer meteorology are increasingly relying on large eddy simulation (LES) models, but few detailed validation studies of these types of models have been done. In this paper we investigate the behavior of an LES model for simulation of a marine boundary layer. Specifically, we focus on the mechanisms which control numerical predictions of entrainment into the tops of marine stratus in a moist generalization of the 1995 GCSS (GEWEX Cloud System Studies) model intercomparison.

For the computational study we present a sequence of simulations of varying resolution, from a typical resolution (50m horizontally and 25m vertically) to a fine resolution (8m horizontally and 4m vertically). We also explore variations in the model such as different subgrid models and modifications of the advection scheme. We do not expect to observe traditional numerical convergence of the solutions under grid refinement; instead we look at various statistical measures of the solution at different resolutions and for variations in the model. We also examine how the structure of the inversion changes with resolution. Finally, we look at the global predictions of entrainment rate and discuss how these predictions relate to the structure of the numerical solutions.

1 Introduction

An important unresolved problem in many areas of boundary layer meteorology is the process of entrainment through a stratified inversion. Large eddy simulations are increasingly used as an alternative to observational data; however, detailed validation of the ability of these models to properly model entrainment through all but the weakest of inversions is limited. This study uses high resolution simulations to examine the role of small scale structures in the entrainment process. In the process, the ability of large eddy simulation to resolve these structures is assessed.

Boundary layer turbulence simulations have been consistently limited by the lack of sufficient computational resources. Although LES models provide a subgrid scale model for unresolved scales, their theoretical foundations require that the large-scale, energy-bearing structures be resolved. Atmospheric flows often contain intrinsic length scales that must be properly resolved for a simulation to be reliable. For example, in the 1995 GCSS model intercomparison study, Bretherton et al. (1998) identified a length scale for a simplified smoke cloud that arises from typical accelerations caused by the density jump at the inversion. For the case they considered this length scale was less than 5m; however, for the intercomparison different models were compared with a nominal resolution of 50m horizontally and 25m vertically. Effectively, the only difference between the compared models was their choice of numerical algorithm and subgrid model. It was found that even for a single class of three-dimensional LES models, entrainment rates and other statistics often differed by a factor of two.

To avoid the computational requirements of 3D modeling, there have been many investigations of idealized entrainment, often in 2D (MacVean and Bretherton 1998; Kuo and Schubert 1988) and with idealized vortices (Siems et al. 1992). Efforts to improve the capabilities of 3D simulations have led to improved numerics (Almgren et al. 1996; Stevens and

Bretherton 1997; Skamarock and Klemp 1994) and subgrid scale parameterizations (Mason and Brown 1994, 1998; Deardorff 1973, 1974, 1980). Recent advances in computational hardware have also made it possible to perform simulations at much finer resolution than was previously possible. Nevertheless, computational studies of boundary layer entrainment using 3D LES models are still underresolved relative to important length scales found in typical flows. The objective of this study is to examine numerical predictions of entrainment in LES simulations for moderately stratified inversions. In particular, we will assess how model predictions depend on resolution, subgrid model and detail of the numerics.

Entrainment in model simulations can come from several sources. Ideally, the model would accurately simulate physical processes, such as overturning of material surfaces pulling air from the stratified free atmosphere into a well-mixed boundary layer or vortical structures in the boundary layer scouring material off top of the inversion, with the subgrid model treating unresolved motions in the inertial range. However, with limited resolution there are also numerical effects, such as numerical diffusion inherent in the method of integration or explicitly added for monotonicity or stability, that can also affect entrainment. Finally, parameterized subgrid scale diffusion where the parameterization attempts to treat large scale motions can also affect entrainment.

A complete understanding of the behavior of a numerical model for simulation of complex turbulent phenomena is a daunting task. To obtain some insight into this behavior we have performed computations over a broad range of resolutions from a nominal resolution of $(\Delta x, \Delta z) = (50\text{m}, 25\text{m})$ to a high resolution with $(\Delta x, \Delta z) = (8\text{m}, 4\text{m})$. The case considered is a moist stratocumulus cloud with evaporative cooling but no buoyancy reversal. The computations use a parallel implementation of the numerical model of Stevens et al. (1999) In addition to changing resolution we also vary the subgrid model and examine a variant of the advection scheme to assess the role of these components of the model on the entrainment behavior. Although we do not expect explicit convergence of the solutions under grid refinement because of the turbulent character of the flow, we can assess various measures of statistical convergence. In particular, we focus on the changes in morphology of the inversion as the grid is refined and discuss how this behavior is modulated by variations in subgrid model and numerics. Finally, we examine the predictions of bulk entrainment and how it depends on the numerics.

The paper is organized as follows. In section 2 we present the model and discuss the variations in subgrid model and the advection discretization. The third section provides the details of the simulations used in the study. Section 4 presents the results of the simulation and discusses the observed trends in the data. We summarize in Section 5 with conclusions and ideas for future work.

2 Model Description

The simulations performed are generalizations of a 1995 GCSS (Bretherton et al. 1998) model intercomparison. The GCSS test case simulated a turbulent boundary layer underneath a strongly stratified inversion. This case was chosen to isolate the effect of longwave radiative cooling on entrainment, by removing condensation and virtual effects on buoyancy. Turbulence was driven solely from radiation, parameterized by a conserved radiatively active tracer that mimicked the effects of cloud radiative cooling. This simplified model intercomparison and made possible comparisons with dry convective boundary layers whose turbulent properties are better understood and documented. However, for many stratus clouds, there is an additional source of turbulence from evaporative cooling. This cooling results from evaporation caused by mixing of saturated boundary layer air at the cloud top with unsaturated, above-inversion air. The mixtures are often less buoyant than their initial sources due to this evaporation.

This study includes this effect by specifying inversion jumps in q_t, the total water mixing ratio and θ_l, the liquid water virtual potential temperature, which, for a given jump in θ_v, the virtual potential temperature, results in the greatest possible evaporative cooling without buoyancy reversal. This corresponds to a value of zero for the stability parameter D as defined by Siems et al. (1990) and 0.23 for the stability parameter K as defined by MacVean and Mason (1990). This jump in inversion values is on the border of the instability region specified by Randall (1973). Although there is a 4 K jump in θ_v at the inversion, roughly 50% of the mixtures are neutrally buoyant with respect to the boundary layer with evaporative cooling exactly canceling the increase in potential temperature from mixing of air from above the inversion.

The model used in this study integrates a modified form of the anelastic equations of Ogura and Phillips (1962). These equations express thermodynamic fields such as the density, ρ, as an isentropic base state $\rho_0(z)$ and a dynamically varying component. As in Clark (1979), we express the dynamic component as the remaining initial environmental deviation in hydrostatic balance $\rho_1(z)$, and a simulated dynamic perturbation ρ_2.

$$\rho(x,y,z,t) = \rho_0(z) + \rho_1(z) + \rho_2(x,y,z,t) \tag{1}$$

This results in the system of equations:

$$\begin{aligned}
\frac{\partial \vec{U}}{\partial t} &= -\frac{\nabla \cdot (\rho_0 \vec{U}\vec{U})}{\rho_0} - \nabla \Pi + g\theta_v^{\#}\vec{k} + H_{\vec{U}}, && (2)\\
\frac{\partial \theta_l^*}{\partial t} &= -\frac{\nabla \cdot (\rho_0 \vec{U}\theta_l^*)}{\rho_0} + H_{\theta_l^*}, && (3)\\
\frac{\partial q_t}{\partial t} &= -\frac{\nabla \cdot (\rho_0 \vec{U} q_t)}{\rho_0} + H_{q_t}, && (4)\\
\nabla \cdot (\rho_0 \vec{U}) &= 0, && (5)
\end{aligned}$$

where Π is the perturbation pressure p_2/ρ_0, $\theta_l^* = (\theta_l - \theta_0)/\theta_0$ is a scaled liquid water potential temperature, and $\theta_v^{\#} = \theta_{v2}/\theta_0$ is a scaled virtual potential temperature buoyancy term. Here, the turbulent stresses and the turbulent fluxes are included in the definitions of H_U, H_{θ^*}, and H_{q_t}. Longwave radiation is parameterized using a simple parameterization.

$$F_r(z) = F_r(H)\exp\left(-K_a \int_z^H \rho_0 q_c dz\right) \tag{6}$$

where H is the height of the domain. Cloud water, q_c, is found by inverting Wexler's equations (Flatau et al 1992) and precipitation is neglected. The subgrid stresses (τ_{ij}) and fluxes ($\overline{u_j'q_t'}, \overline{u_j'\theta_l^{*\prime}}$) are computed using a subgrid model.

One issue we will address is the degree to which mixing in a simulation is governed by the form of the subgrid model used in the simulations. We consider three different options for the subgrid model. The first is to use a variation of the turbulent kinetic energy (TKE) 1.5-order closure scheme (Deardorff 1974), the second is to use the Smagorinsky/Lilly 1.0-order scheme (Lilly 1962; Smagorinsky 1963), and the third option is to use no explicit subgrid model.

The TKE scheme is derived by averaging the momentum equations about a length scale determined by the model resolution. It involves a prognostic equation for the subgrid energy, e_{tke}, that includes terms for production by deformation and buoyancy and its dissipation.

$$\frac{\partial e_{tke}}{\partial t} + u_k \frac{\partial e_{tke}}{\partial x_k} = K_m \mathrm{Def}^2 + \frac{2}{\rho_0}\frac{\partial}{\partial x_k}\rho_0 K_m \frac{\partial e_{tke}}{\partial x_k} - K_h N^2 - c_\epsilon \frac{e_{tke}^{3/2}}{l}. \tag{7}$$

Here, K_m is the eddy viscosity, $\mathrm{Def}^2 = 2S_{ij}S_{ij}$ is the deformation squared, $S_{ij} = \frac{1}{2}(\frac{\partial u_i}{\partial x_j} + \frac{\partial u_j}{\partial x_i})$ is the strain tensor and N^2 is a local estimate of the Brunt-Vaisala frequency. The term $\frac{2}{\rho_0}\frac{\partial}{\partial x_k}\rho_0 K_m \frac{\partial e_{tke}}{\partial x_k}$ parameterizes triple moment terms. Eq. (7) contains the length scale assumptions:

$$K_h = c_h l e_{tke}^{\frac{1}{2}}, \tag{8}$$

$$K_m = c_m l e_{tke}^{\frac{1}{2}}, \tag{9}$$

where the length scale $l = (\Delta x \Delta y \Delta z)^{1/3}$. This length scale is not corrected for stability or condensation effects.

The Smagorinsky subgrid model is derived by making the additional assumption that e_{tke} is in local equilibrium,

$$0 = K_m \mathrm{Def}^2 - K_h N^2 - c_\epsilon \frac{e_{tke}^{3/2}}{l}, \tag{10}$$

which, after eliminating e_{tke}, yields the eddy viscosity.

$$K_m = c_s^2 l^2 \mathrm{Def}\sqrt{1 - Ri/Pr}, \quad c_s^4 = c_m^3/c_\epsilon. \tag{11}$$

Here $Pr = c_m/c_h$ is a Prandtl number and $Ri = N^2/\mathrm{Def}^2$ is a flux Richardson number. An interesting property of the Smagorinsky subgrid model is that for large Richardson numbers, $Ri > Pr$, $e_{tke} = 0$, whereas for the TKE model, e_{tke} is often nonzero under identical conditions. The difference between these two models is that one assumes local whereas the other assumes nonlocal subgrid kinetic energy. The values of the nondimensional constants are the neutral values $(c_m, c_h, c_\epsilon, c_s) = (0.15, 0.38, 0.93, 0.25)$. It should be noted that there is some ambiguity about appropriate values of these coefficients, especially in the presence of condensation. Another caveat is the choice of length scale. Here it is tied only to an estimate of the mesh resolution. Other researchers tie it to different estimates such as the horizontal resolution and often add stability and condensation dependencies. This is an area of active research, as recent experience has shown that varying c_s by a factor of two can completely change the character of convection in certain atmospheric simulations. Here it is meant only to relate a typically configured choice of subgrid models to documented numerical methods. As an additional test of the role of the subgrid model we also performed computations without the subgrid model. (This is possible because of the high-resolution upwind methodology used for the advection scheme. Similar results would be obtained with other TVD-type schemes; however, for discretizations such as central difference approximations the lack of a subgrid model could lead to unacceptable oscillations in the solution.)

The numerical model used in this study was developed by Almgren et al. (1998), modified to use an advection scheme and treatment of physical processes developed by Stevens and Bretherton (1997) and Smolarkiewicz and Margolin (1995). For a detailed description of the numerical model, see Stevens et al. (1999) which includes the treatment of adaptive mesh refinement. In this paper, we use a distributed memory single-level version of the adaptive algorithm based on the parallel framework developed by Rendleman et al. (1999). The discretization is a forward-in-time projection method using a 3rd order advection scheme for both velocity and scalar advection. This advection scheme has better accuracy properties than many commonly used schemes in meteorological models.

The advection scheme used in this study uses a slope-limiting procedure to limit oscillations in the solution. The slope-limiting effectively adds dissipation near underresolved gradients which gives the advection scheme performance characteristics similar to the TVD scheme used by Shutts and Gray (1994). Slope limiting is used for both q_t and θ_l and prevents spurious oscillations in these fields. For the momentum transport, slope limiting is optional. The comparison of computations with and without slope limiting for momenta allows us to evaluate the effects of minor differences in the advection scheme on the entrainment process.

3 Simulation Cases

As noted above, this study includes the effect of moisture by specifying inversion jumps in q_t and θ_l which, for a given jump in θ_v, result in the greatest possible evaporative cooling without buoyancy reversal. The initial profiles and typical hourly averages for q_t and θ_l are shown in Figure 1. The jumps in q_t and θ_l are similar in magnitude to those observed in Nicholls and Turton (1983), although the resultant cloud is deeper and thicker, as seen by the profile of q_c, the mixing ratio of condensed water, in Figure 1. The initial profiles of q_t and θ_l were chosen to be smooth to ensure that details of the initialization were resolved on the coarsest grid. The radiative cooling S_{rad} which drives the simulations was parameterized using constant values of $F_r(H) = 100$ Wm^{-2} and $K_a = 10$ m^2 kg^{-1}. This results in most of the radiative forcing being concentrated with 70m of the inversion, as seen in Figure 1. The winds were initially calm and no large scale forcings such as subsidence were applied. Motions were initiated via perturbations in θ_l and e_{tke} consisting of fixed sums of sine waves with random amplitudes and phases. The maximum amplitudes were 0.1K and 10^{-3}m^2 s^{-2}, respectively. The domain was 3.2km wide in each horizontal dimension and 1.2km high.

Several experiments were conducted using the simulations summarized in Table 1. These experiments were used to compare the role of resolution, numerics and subgrid model. Accordingly, the simulations are given acronyms composed of the resolution used: L (50m $\times$ 50m$\times$25m), M (25m$\times$25m$\times$12.5m), H (12.5m$\times$12.5m$\times$6.25m), and V (8m$\times$8m$\times$4m); the value of l used in the subgrid model, whether slope-limiting was used on the momenta (S), and the order of the subgrid model. For instance, the simulation **L40S_10** is a low resolution simulation using a length scale of 40m, slope-limiting and the Smagorinsky subgrid model. All of the statistics reported in this section are hourly averages centered at 2.5 hours, except where noted. At 2.5 hours, initial transients from the random initialization had died out and it was possible to generate stable turbulence statistics as shown by the time series of the convective velocity scale

$$w^* = 2.5 \int_0^{z_{inv}} g\overline{w\theta_v^\#} dz \tag{12}$$

where $\overline{w\theta_v^\#}$ represents a horizontal average of the buoyancy flux over the entire domain, displayed as a running 5 minute average (Figure 2). The equilibrium character of the statistics was further confirmed by examining linear flux profiles which are not shown. Figure 2 indicates that buoyancy production had stabilized after roughly 4000s of simulation. A summary of w^* and other hourly averaged statistics are presented in Table 2.

4 Computational Results

In this section we present results of the computational study described above. The simulations are highly turbulent and we do not expect to observe convergence in a traditional point-wise sense. Instead, we will look for statistical measures of convergence and evaluate the ability of the simulations to capture average behavior of the solutions. We will also examine the structure of the solution as the mesh is refined to explore trends in the data and study the dependence of solutions on subgrid model and details of the numerical method.

Finally, we will look at the implication of the results for predicting entrainment rates such as might be used in parameterizations of entrainment behavior.

Initially, we will focus our analysis of the computational results on the behavior of q_t, the total water mixing ratio. The vertical profiles obtained by averaging q_t horizontally and in time as depicted in Figure 1 are insensitive to resolution, numerics and subgrid model. One statistic which provides a global measure of the variability of the simulations is the profile of the moisture fluctuations $\left\langle \overline{q_t'^2} \right\rangle^{1/2}$ shown in Figure 3. These profiles show a strong dependence on resolution with the variations concentrated between 700m and 800m. The higher-resolution simulations have stronger q_t perturbations indicating greater variability with increased resolutions. Furthermore, the profile appears to be converging as resolution is increased with little dependence on either the subgrid model or the details of the numerics.

To assess the dependence of small scale structures on resolution in more detail we examine the instantaneous structure of q_t after 2 hours of simulation. Figure 4 displays typical cross sections for **L40_15, M20_15, H10_15** and **VO6_15** over a vertical range of .5 km to 1.km. (Each cell is plotted as a rectangle whose size is determined by resolution and color by cell value.) Only at the finer resolutions do we begin to see overturning of mixed values. Although the inversion is remarkably flat, most of the tongues of entraining fluid extend to depths of 50-100m and do not appear to depend strongly on resolution. However, we observe that as resolution increases these tongues thin and their number increases.

To analyze the local structure in more detail, we must first define the inversion more precisely. First, we define the boundary layer height, z_{inv}, to be the uppermost location of the contour $q_t = 8.5$g kg^{-1}. We then define the thickness of the inversion layer, δz_{inv} to be the thickest contiguous portion of a vertical column for which $7.5 \leq q_t \leq 8.5$ (g kg^{-1}). The values of 7.5 and 8.5 g/kg represent the middle third of the jump between inversion and boundary layer values. (We note that the definition of inversion thickness we are using is different than the estimate used in the GCSS intercomparison, which used the standard deviation of the boundary layer height as a measure of the inversion layer.) In Figure 5, the layer defining δz_{inv} is plotted for cross-sections in Figure 4 with an expanded vertical scale. The difference in appearance between Figures 4 and 5 is due, in part, to the sharp cutoff value defining the layer and reflects the definition of the inversion depth given above. Figure 5 illustrates that most of the inversion occupies a thin layer that is shrinking to a scale of less than 10m. Regions where entraining tongues occur thicken to a depth of roughly 50m.

The horizontal average of the thickness of this layer, denoted $\overline{\delta z}_{inv}$, can be used as a measure of inversion thickness to estimate the depth of the layer where the strongest mixing of inversion and boundary layer air occurs. The average depth of the layer is tabulated in Table 2 and shown in Figure 6. For the four cases presented, we can fit the data with the relation

$$\overline{\delta z}_{inv} = (5.4) + (0.22)(l)^{(1.07)}. \tag{13}$$

This indicates that the average thickness of the inversion layer is converging with first-order accuracy in the mesh spacing to a value of 5.4m. In particular, this suggests that under continued refinement the inversion thickness does not go to zero but converges to a finite value.

We want to explore in more detail how the structure of the inversion changes with increasing resolution. In Figure 7, snapshots of δz_{inv} after 2 hours of simulation are presented for **L40_15, M20_15, H10_15** and **VO6_15**. As the resolution is increased we observe that the structure of the downwellings becomes increasingly fine, and the regions between the downwellings become increasingly thin.

In order to quantify these differences, we measure statistical properties of the downwelling regions. In particular, we look at clusters of neighboring columns of downwellings of mixing air where δz_{inv} is greater than 50 m. For the coarsest simulations such as **L40_15**, this is equivalent to 2 vertical mesh spacings.

In Figures 8, 9, and 10, hourly statistics are computed for the number of clusters, the average area of the clusters and the average depth of the clusters. The data indicate a number of interesting features. First, as the resolution is increased, the number of downwelling clusters increases and the average area each cluster occupies decreases, both rather dramatically. We note that although the average area of each event is relatively insensitive to the subgrid model or the numerics, the number of clusters shows some dependence on both of these factors. The simulations without a subgrid model or limiting have the most clusters with the non-slope limiting cases having the next most and the slope-limiting cases have the fewest. Thus, the number of downwellings appears to correlate inversely with the amount of dissipation in the numerical model. Another interesting observation is that the average depth of the downwelling events is relatively insensitive to resolution, numerics or subgrid model, having values in the 73-79m range for all of the simulations.

The behavior of the number of clusters with both resolution and choice of subgrid method and details of the numerics suggests that the number of clusters is related to the ability of the simulation to represent steep gradients. The deformation provides a more explicit estimate of the representation of steep gradients that can sustain small scale motions in the flow. The average value of the deformation in the boundary layer is shown in Figure 11. As with the number of clusters, the deformation is strongly resolution-dependent, but with a trend showing the least dissipative simulations having larger average deformation at a given resolution.

The dependence of the morphology of the inversion can also be seen in the power spectra of vertical velocities at both the center of the boundary layer and at the inversion. Figure 12 shows the spectra for all of the resolutions with the TKE model and no slope-limiting. In the boundary layer, as the mesh is refined we see less energy in the low wave numbers and a slight shift of the spectrum to the right. At the inversion, we also see less energy in low wave numbers on coarser grids. We also observe that at the inversion there is a peak frequency in the power spectrum that shifts to the right as the resolution increases. This dominant frequency is related to the size of eddies at the inversion and its behavior with resolution suggests that the eddies are becoming smaller as the mesh is refined.

Having examined the structure of the solution at varying resolution, we look at the ability of the simulations to predict quantities of meteorological importance for parameterizing entrainment. One of the most fundamental is the entrainment rate, defined as the time derivative of the inversion height, $w_e = \frac{\partial z_{inv}}{\partial t}$. The data for the simulations are presented in Table 2 and graphed in Figure 13. The most dramatic feature of the data is that the entrainment rate depends more strongly on the details of the numerics than on the resolution. The simulations with no slope-limiting or subgrid model entrain the most; the simulations with both entrain the least. The most dramatic effect is whether the numerics includes slope limiting, which suggests that the details of the numerics play a key role in predicting entrainment rate.

A relationship between the magnitude of boundary layer motions and entrainment is a fundamental part of parameterizing the entrainment. A useful quantity for analyzing this relationship is the fraction A of the net boundary layer buoyancy production available for driving entrainment. This relationship is often given by the parameterization

$$w_e/w^* = A/Ri, \tag{14}$$

$$Ri = \frac{g z_{inv} \Delta\theta_v}{\theta_0 w^{*2}}. \tag{15}$$

Typically for a dry convective boundary layer driven by surface heating, A has a value around 0.2. This parameterization appears to hold for the dry smoke cloud of the 1995 intercomparison but with a larger value of $A \approx 0.4 - 0.6$. This indicates that the radiatively driven case is more effective at converting boundary layer buoyancy production into entrainment than a normal convective boundary layer.

A provides an estimate of the degree to which varying resolution, numerics, and subgrid model alter the fraction of buoyancy production available for entrainment. The behavior of the parameter, A, is shown in Figure 14. Again, we see that A is relatively insensitive to the spatial resolution and depends most strongly on the details of the numerics. The computations with slope limiting, which are more dissipative, predict a lower value of A than the other simulations.

The insensitivity of the entrainment rate w_e and the parameter A on the resolution in spite of the strong dependence of the morphology of the inversion suggest that these quantities are controlled by an interplay of different effects that have opposite and competing trends as the resolution is increased. To shed some light on this issue, we plot, in Figure 15, the power spectra for vertical velocity for all of the medium resolution (M) simulations. For a given resolution, the boundary layer spectra are all very similar with respect to numerics and choice of subgrid model. This indicates that the behavior in the boundary layer is not driving the disparity of results seen in Figures 13 and 14.

The situation at the inversion is decidedly different. There we see a dominant frequency with a peak value that depends strongly on the choice of numerics and subgrid model. In particular, the height of the peak correlates directly with both the w_e and A. This indicates that the choice of numerical and subgrid model influences the strength of the dominant eddies and that this strength is a key factor in determining the entrainment rate and A.

5 Conclusions

It is clear that even at the finest resolution the simulations presented here are underresolved. Thus they cannot be viewed as definitive, but do, nevertheless, suggest several conclusions about numerics, subgrid models and resolution for these types of problems.

First, inversion structure is clearly a function of resolution. As resolution increases, increasingly fine structure in the downwellings and an overall thinning of the inversion become evident. Interestingly, the average inversion thickness appears to be converging to a finite nonzero value as the mesh is refined. Another interesting feature is that the thickness of the downwelling events is insensitive to resolution, subgrid model or numerics.

Second, in this underresolved regime, the entrainment rate depends more strongly on the choice of subgrid model and the details of the numerics, particularly the latter, than on the resolution. The amount of entrainment is related to both the number of downwelling events and their average area. These effects are competing and roughly cancel as resolution is increased. The strength of the entraining eddies, as measured by the power spectra of velocity, plays a key role in determining the net entrainment. We also emphasize that in this interplay, the particular choice of subgrid model is less significant than numerics.

This study raises more questions than it answers. There are a number of important length scales in this problem and it remains unclear which scales are most important for properly simulating entrainment. A study by Lewellen and Lewellen(1998) suggests that properly resolving the ability of turbulence in the boundary layer to perform work is the key to accurately simulating the evolution of these clouds. However, although the thickness of the boundary layer, $z_{inv} = 700$m, is quite large, the velocity spectra in the boundary layer suggest that the relevant structures in the boundary layer are much smaller. Another viewpoint arises from the idea that entrainment is primarily a function of the net source of kinetic energy (Lock and MacVean 1997). In this case study, the sources are limited to radiation with the bulk of it contained within 100 m of the inversion; however, an additional study in which the depth of penetration of the radiation was varied would be required to draw definitive conclusions about the role of this length scale. Another scale identified by Bretherton et al. (1998) and Stevens and Bretherton (1999) is the undulation length scale,

$$\delta z_u = z_{inv}/Ri. \tag{16}$$

This length scale is an estimate of the distance it takes a buoyancy force representative of the inversion strength to slow an air parcel from w^* to zero. For the problem considered here, that length scale is 7m which is close to the estimated inversion thickness of 5.4m. Again, additional studies with varying initial conditions would be needed to see if these length scales remained correlated.

The dependence of entrainment rates and entrainment efficiency on the details of the numerical algorithm is somewhat distressing. A more comprehensive study involving a broad range of numerical approaches is needed to more clearly delineate this issue. One would like to hope that as resolution is increased the dependence on the details of numerics and subgrid model would decrease. The data also offer some hope for the future. The thickness of the inversion does not appear to be approaching zero as the mesh is refined. If we could perform simulations at 1m resolution, we could reasonably expect to accurately resolve the inversion, which would hopefully lead to a dramatic improvement in entrainment estimates for this type of simulation.

Acknowledgments

This work was supported by the Defense Special Weapons Agency IACRO98-3017, through the U. S. Department of Energy under Contract DE-AC03-76SF00098.

References

Almgren, A. S., J. B. Bell, and W. G. Szymczak, 1996: A numerical method for the incompressible Navier-Stokes equations based on an approximate projection. *SIAM J. Sci. Comput.*, **17**(2).

Almgren, A. S., J. B. Bell, P. Colella, L. H. Howell, and M. L. Welcome, 1998: A Conservative Adaptive Projection Method for the Variable Density Incompressible Navier-Stokes Equations, *J. Comp. Phys.*, **142**, 1-46.

Bretherton, C. S., M. K. MacVean, P. Bechtold, A. Chlond, W. R. Cotton, J. Cuxart, H.

Cuijpers, M. Khairoutdinov, B. Kosovic, D. Lewellen, C. H. Moeng, P. Siebesma, B. Stevens, D. E. Stevens, R. I. Sykes, and M. C. Wyant, 1998: An intercomparison of radiatively-driven entrainment and turbulence in a smoke cloud, as simulated by different numerical models. *Quart. J. R. Meteor. Soc.*, To Appear.

Clark, T. L., 1979: Numerical Simulations with a Three-Dimensional Cloud Model: Lateral Boundary condition experiments and multicellular severe storm simulations. J. Atmos. Sci., **36**, 2191-2215.

Deardorff, J. W., 1973: The use of subgrid transport equations in a three-dimensional model of atmospheric turbulence. *J. Fluids Eng.*, **95**, 429-438.

Deardorff, J. W., 1974: Three-dimensional numerical study of turbulence in an entraining mixed Layer. *Bound.-Layer Meteor.*, **7**, 199-226.

Deardorff, J. W., 1980: Cloud-top entrainment instability *J. Atmos. Sci.*, **37**, 131-147.

Flatau, P.J., R. L. Walko, and W. R. Cotton, 1992: Polynomial fits to saturation vapor pressure. *J. Appl. Met.*, **31**, No. 12, 1507-13.

Kuo, H., and W. T. Schubert, 1988: Stability of cloud-topped boundary layers. *Quart. J. R. Meteor. Soc.*, **114**, 887-916.

Lewellen, D. C., and W. S. Lewellen, 1998: Large eddy boundary layer entrainment. *J. Atmos. Sci.*, Submitted.

Lilly, D. K., 1962: On the numerical simulation of buoyant convection. *Tellus*, **14**, 148-171.

Lock, A. P., and M. K. MacVean, 1997: The parameterization of entrainment driven by surface heating and cloud-top cooling. *Quart. J. R. Meteor. Soc.*, Submitted.

MacVean, M. K., and C. S. Bretherton, 1998: Boundary-layer cloudiness and cloud-top entrainment instability – a new synthesis. *Quart. J. R. Meteor. Soc.*, Submitted.

MacVean, M. K., and P. J. Mason, 1990: Cloud-top entrainment instability through small-scale mixing and its parameterization in numerical models, *J. Atmos. Sci.*, **47**, 1012-1030.

Mason, P. J., and A. R. Brown, 1994: The sensitivity of large-eddy simulations of turbulent shear flow to subgrid models. *Bound. Layer Meteor.*. **70**, 133-150.

Mason, P. J., and A. R. Brown, 1998: On Subgrid models and filter operations in large-eddy simulations. *J. Atmos. Sci.*, Provisionally Accepted.

Nicholls, S., and J. D. Turton, 1986: An observational study of the structure of stratiform cloud sheets: Part II. Entrainment. *Quart. J. R. Meteor. Soc.*, **112**, 461-480.

Ogura, Y., and N. Phillips, 1962: Scale Analysis of Deep and Shallow Convection in the Atmosphere. *J. Atmos. Sci.*, **19**, 173-179.

Rendleman, C. A., V. E. Beckner, M. Lijewski, W.Y. Crutchfield, and J. B. Bell, 1999: A Parallel Adaptive Mesh Refinement Algorithm for Hyperbolic Systems of Conservation Laws. In Preparation.

Randall, D. A., 1980: Conditional instability of the first kind upside-down. *J. Atmos. Sci.*, **37**, 125-130.

Siems, S. T., C. S. Bretherton, M. B. Baker, S. Shy, and R. E. Breidenthal, 1990: A numerical investigation of cloud-top entrainment instability and related experiments. *Quart. J. R. Meteor. Soc.*, **118**, 787-818.

Skamarock, W. C., and J. B. Klemp, 1993: Adaptive grid refinement for two-dimensional and three-dimensional nonhydrostatic atmospheric flow. *Monthly Weather Review*, **121**, 788-804.

Smagorinsky, J., 1963: General circulation experiments with the primitive equations: 1. The basic experiment. *Monthly Weather Review*, **91**, 99-164.

Smolarkiewicz, P. K. and L. G. Margolin, 1993: On forward-in-time differencing for fluids:

extension to a curvilinear framework. *Monthly Weather Review*, **121**, 1847-1859.

Stevens, B. C. H. Moeng, and P. P. Sullivan, 1998: Subgrid sensitivities in large-eddy simulations of radiatively driven convection. *J. Atmos. Sci.*, submitted.

Stevens, D. E. and C. S. Bretherton, 1997: A forward-in-time advection scheme and adaptive multilevel flow solver for nearly incompressible atmospheric flow. *J. Comput. Phys.*, **129**, 284-295.

Stevens, D. E. and C. S. Bretherton, 1999: Effects of Grid Resolution on Large-Eddy Simulation of Radiatively Driven Entrainment Through A Strong Inversion. Quart. J. Roy. Met. Soc.. To Appear.

Stevens, D. E., A. S. Almgren,and J. B. Bell, 1999: Adaptive simulations of trade cumulus convection, *Mon. Wea. Rev.*, submitted for publication.

Figure Captions

Figure 1: Initial Conditions (solid). 1 hour averages centered at: dotted, 30 minutes; dash-dot, 90 minutes; and dashed, 150 minutes. S_{rad} is the radiative flux divergence.

Figure 2: w^* as a function of time. Line types are determined by resolution L (dot), M (dash), H (solid), and V (dash-dot).

Figure 3: $\left(\overline{q_t'^2}\right)^{1/2}$ at the inversion. Line types are determined by resolution L (dot), M (dash), H (solid), and V (dash-dot).

Figure 4: qt cross section in (g kg^{-1}) at t = 2 hours. L40_15 (top), M20_15 (upper middle), H10_15 (lower middle), and V06_15 (bottom).

Figure 5: Cross section showing δz_{inv} at t = 2 hours. This quantity is a measure of boundary layer thickness. L40_15 (top), M20_15 (upper middle), H10_15 (lower middle), and V06_15 (bottom).

Figure 6: $\overline{\delta z}_{inv}$ and average area of downwellings (B) as a function of resolution. Line types are determined by subgrid model used: none (dots), Smagorinsky (solid) and TKE (dashs).

Figure 7: δz_{inv} for each resolution at t = 2 hours. (top left, L40_15; top right, M20_15; bottom left, H10_15; bottom right, V06_15)

Figure 8: Average number of downwellings. Line types are defined as in Figure 6.

Figure 9: Average area of downwellings. Line types are defined as in Figure 6.

Figure 10: Average depth of downwellings. Line types are defined as in Figure 6.

Figure 11: Boundary layer deformation. Line types are defined as in Figure 6.

Figure 12: Sensitivity of power spectra of w to resolution. Spectra denoted by + symbols are

calculated from data at the inversion. Spectra without the + symbols are calculated from data at the middle of the boundary layer. Line types are determined by resolution: (dots) L40_15, (dash-dot) M20_15, (dash) H10_15, and (solid) V06_15.

Figure 13: Entrainment rate, w_e. Line types are determined by subgrid model used: none (dots), Smagorinsky (solid) and TKE (dashs). Data points are labeled with the order of their subgrid model and are preceded by an S when slope-limiting is present.

Figure 14: The A parameter. Line types are defined as in Figure 13.

Figure 15: Sensitivity of power spectra of w to numerics. Spectra denoted by + symbols are calculated from data at the inversion. Spectra without the + symbols are calculated from data at the middle of the boundary layer. Line types are determined by simulation group: (dots) no slope-limiting and subgrid model, (solid) no slope limiting but with subgrid model, (dash) slope limiting but no subgrid model (dash-dot) slope limiting and subgrid model.

Table Captions

Table 1: Simulation names are a combination of smoke (S), resolution (L,M,H,V), Smagorinsky length scale ($l = (\Delta x \Delta y \Delta z)^{1/3}$) in meters, slope limiting (S_) and the order of the subgrid model. TKE and SMAG are acronyms for the turbulent kinetic energy and Smagorinsky subgrid models respectively.

Table 2: Simulation parameters after 2.5 hours of simulation.

Simulation	slopes	sgs	NX	NZ	Δx (m)	Δz (m)	l (m)
L00S_00	yes	none	64	48	50.00	25.00	40
M00S_00	yes	none	128	96	25.00	12.50	20
H00S_00	yes	none	256	192	12.50	6.25	10
L40S_15	yes	TKE	64	48	50.00	25.00	40
M20S_15	yes	TKE	128	96	25.00	12.50	20
H10S_15	yes	TKE	256	192	12.50	6.25	10
L00_00	no	none	64	48	50.00	25.00	40
M00_00	no	none	128	96	25.00	12.50	20
H00_00	no	none	256	192	12.50	6.25	10
L40_10	no	SMAG	64	48	50.00	25.00	40
M20_10	no	SMAG	128	96	25.00	12.50	20
H10_10	no	SMAG	256	192	12.50	6.25	10
L40_15	no	TKE	64	48	50.00	25.00	40
M20_15	no	TKE	128	96	25.00	12.50	20
H10_15	no	TKE	256	192	12.50	6.25	10
V06_15	no	TKE	400	300	8.00	4.00	6

Table 1:

Simulation	A	w_e (mm/s)	w^* (m/s)	δz_u (m)	δz_{inv} (m)
L00S_00	1.00	9.56	1.01	7.19	16.53
M00S_00	1.02	9.59	1.00	7.09	10.91
H00S_00	1.01	9.71	1.01	7.22	7.89
L40S_15	1.02	9.32	1.00	7.02	16.63
M20S_15	1.00	9.41	1.01	7.11	10.74
H10S_15	1.04	9.63	1.00	7.04	7.97
L00_00	1.13	10.69	1.00	7.23	17.29
M00_00	1.23	11.27	0.99	7.00	11.15
H00_00	1.19	11.41	1.00	7.23	8.13
L40_10	1.12	10.57	1.00	7.20	17.06
M20_10	1.13	10.55	1.00	7.09	10.97
H10_10	1.15	10.85	1.00	7.15	8.01
L40_15	1.13	10.62	1.00	7.18	17.12
M20_15	1.13	10.42	0.99	7.03	10.93
H10_15	1.19	11.03	0.99	7.08	8.17
V06_15	1.22	11.07	0.99	7.00	6.82

Table 2:

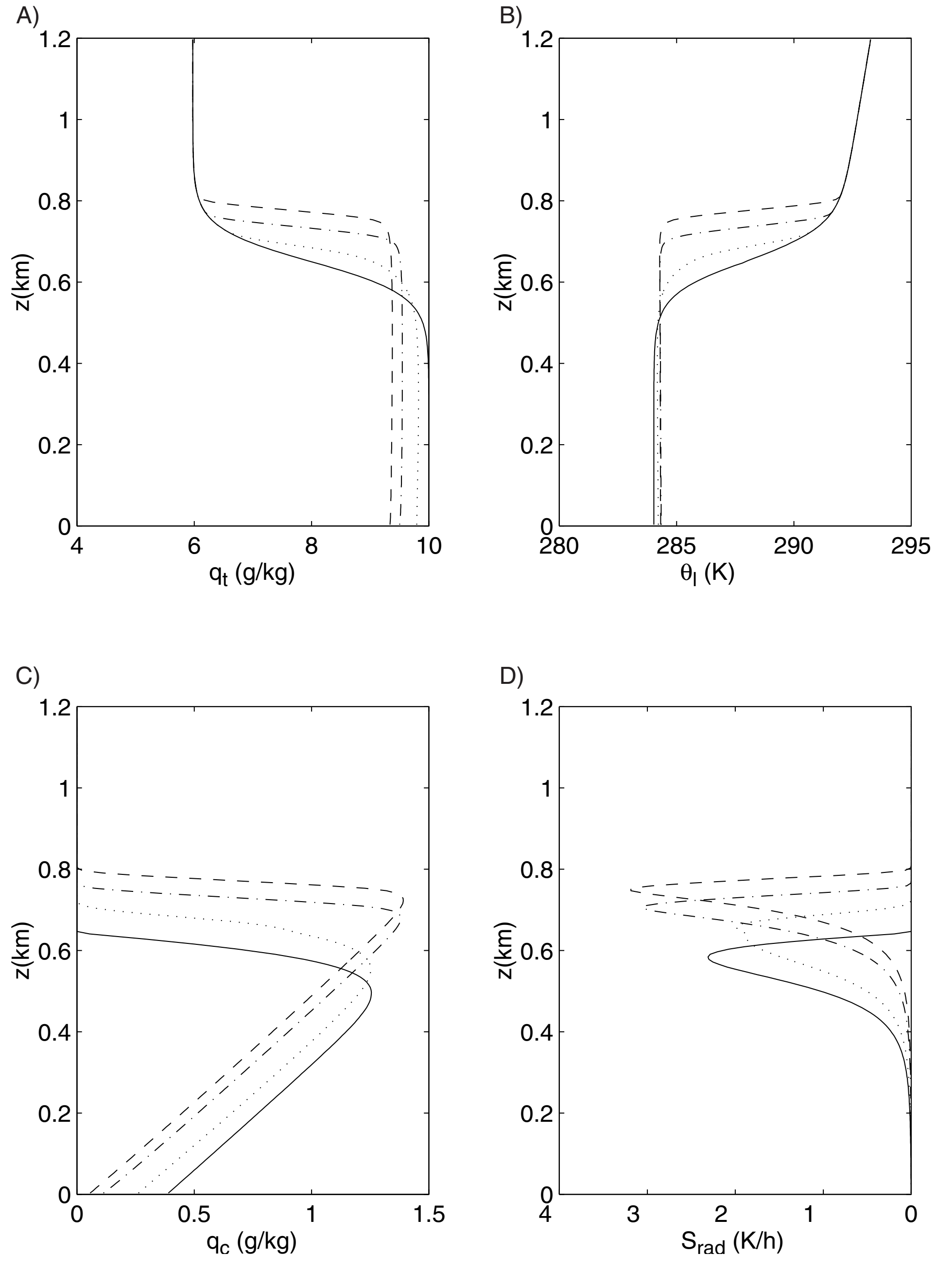

Figure 1:

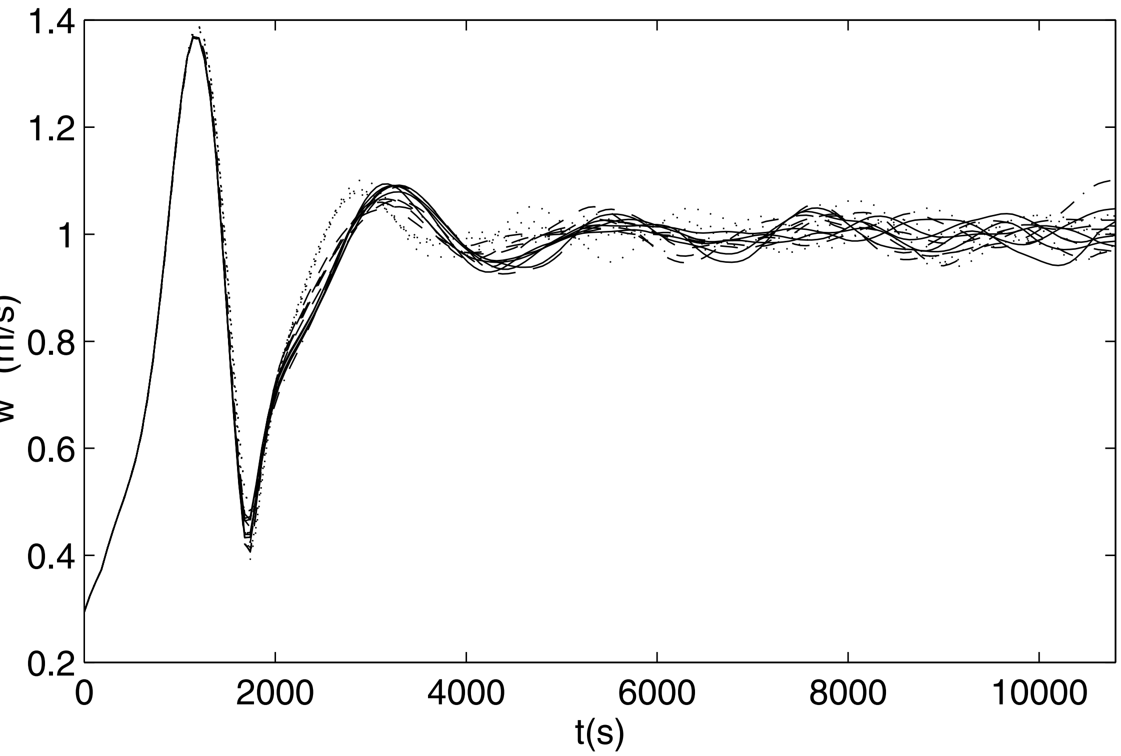

Figure 2:

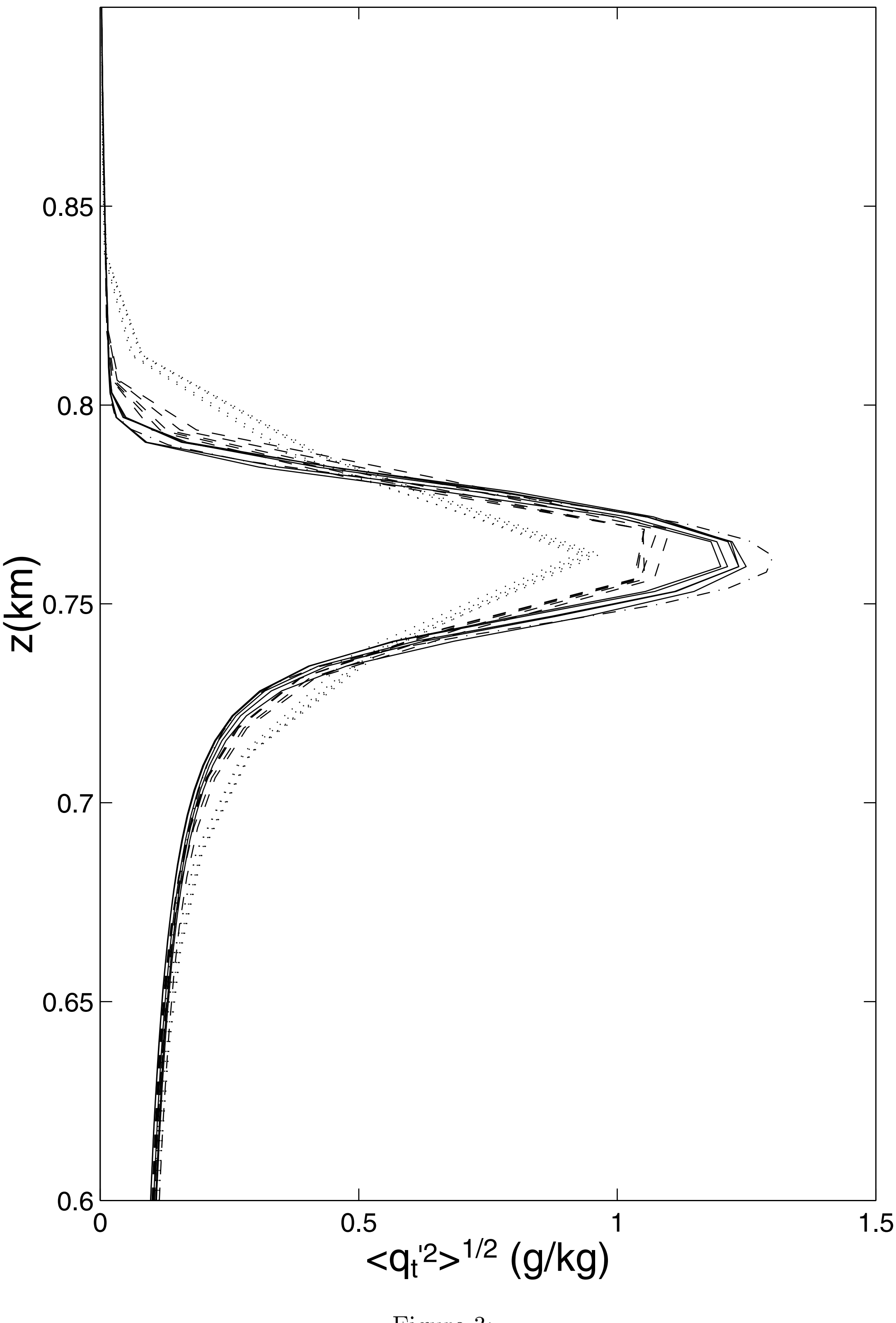

Figure 3:

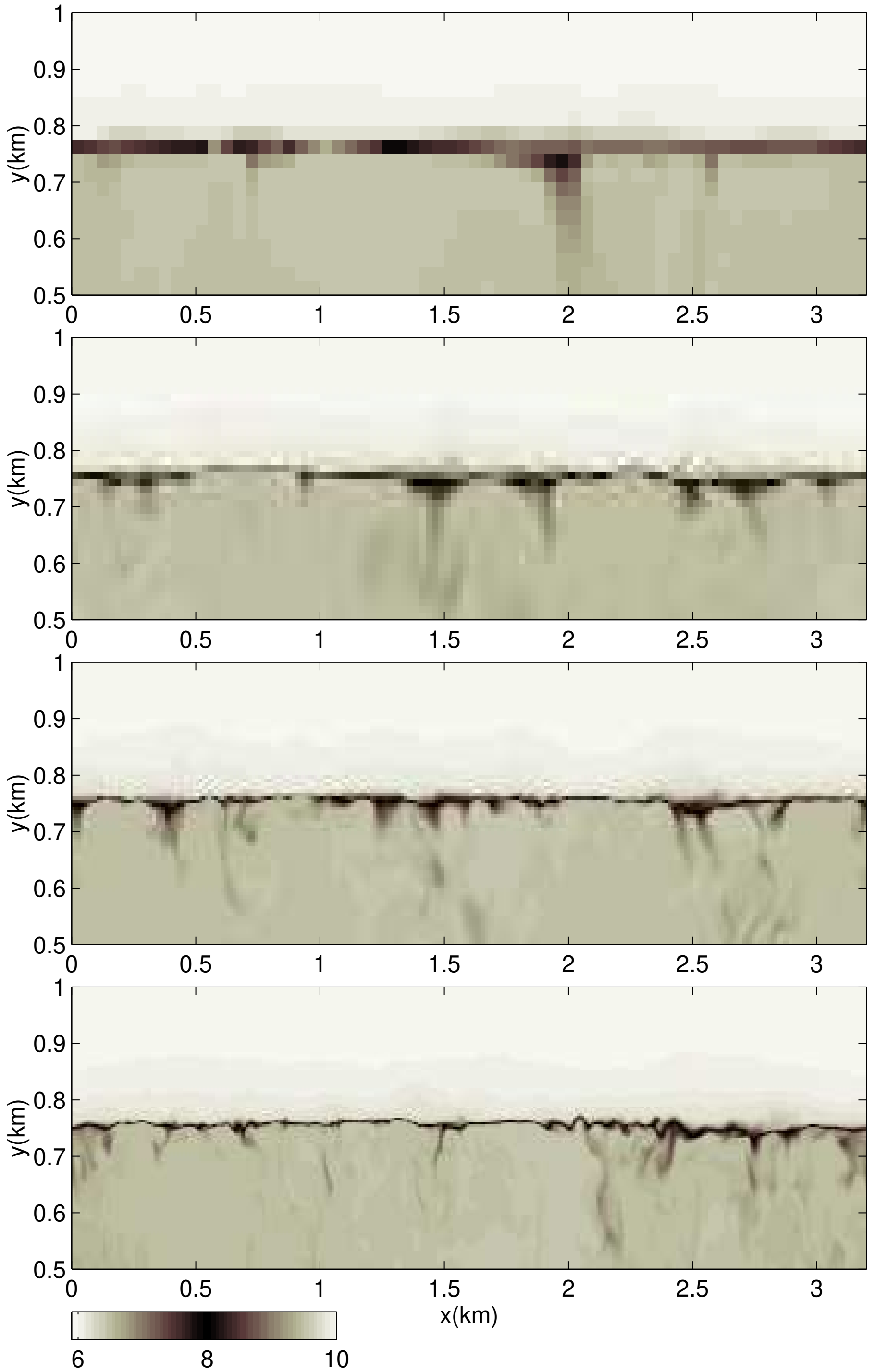

Figure 4:

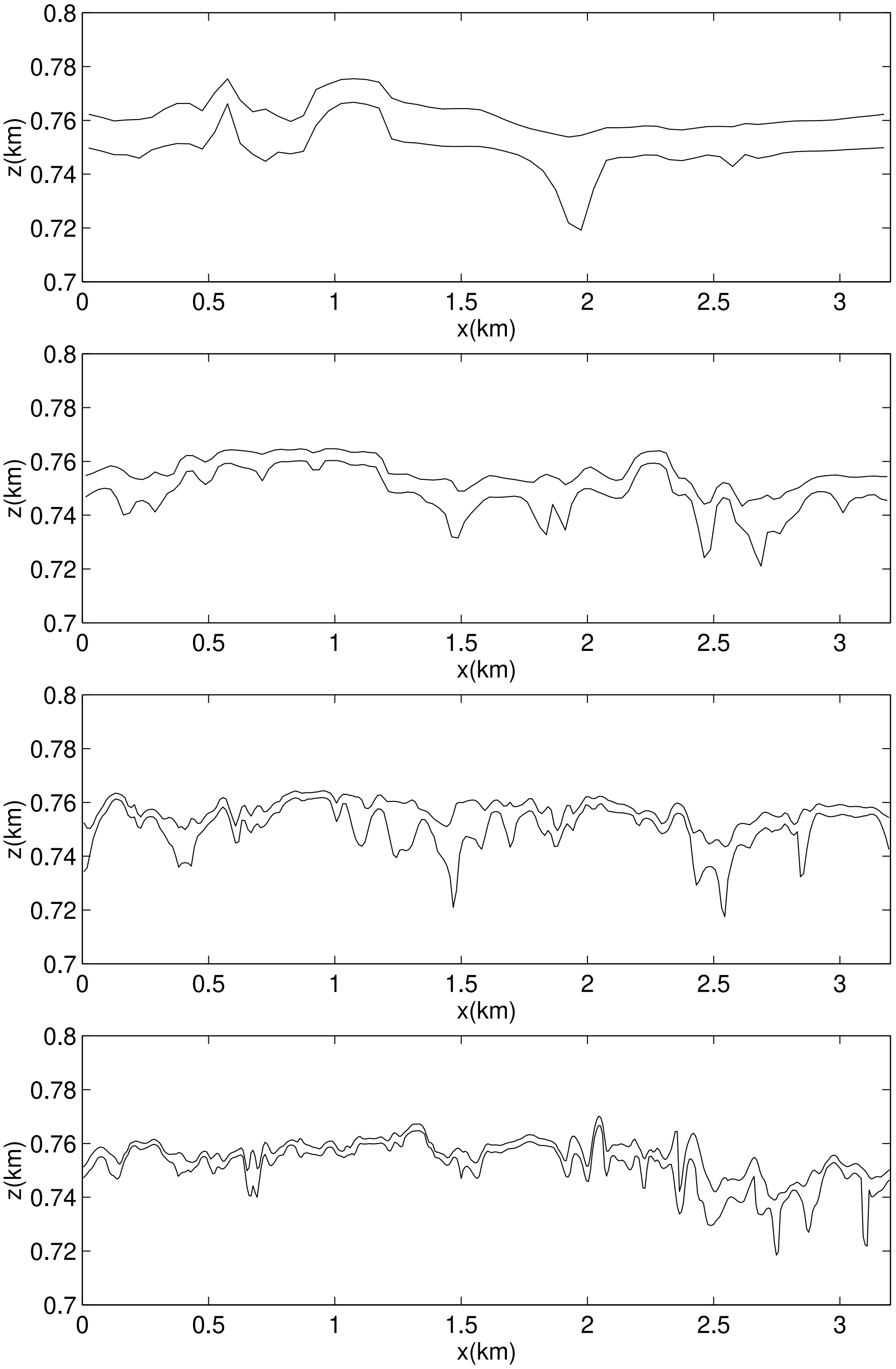

Figure 5:

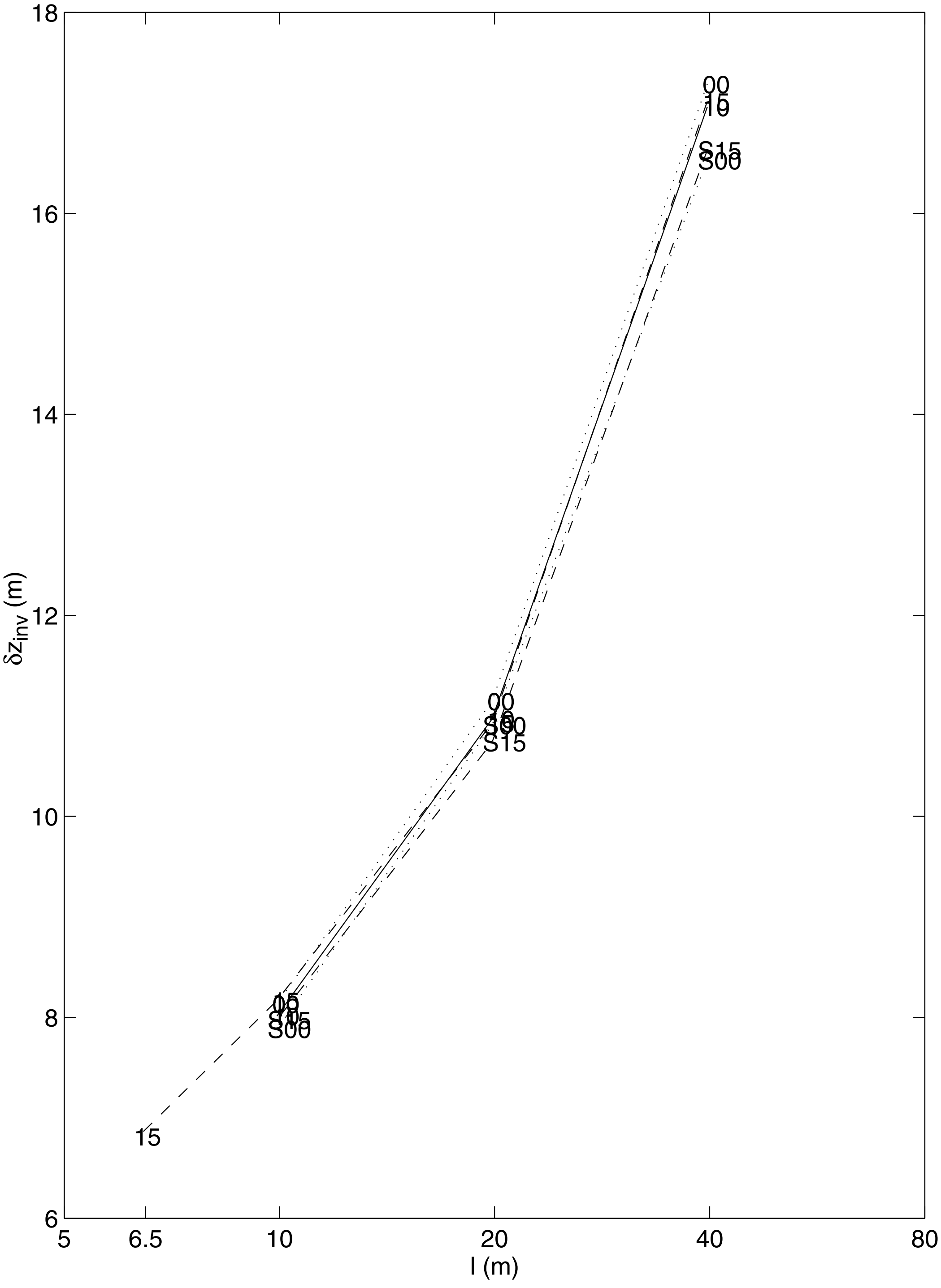

18
16
14
12
10
8
6
δz_{inv} (m)
5
6.5
10
20
40
80
l (m)
00
15
10
S15
S00
00
15
S00
S15
15
00
S15
S00
15

Figure 6:

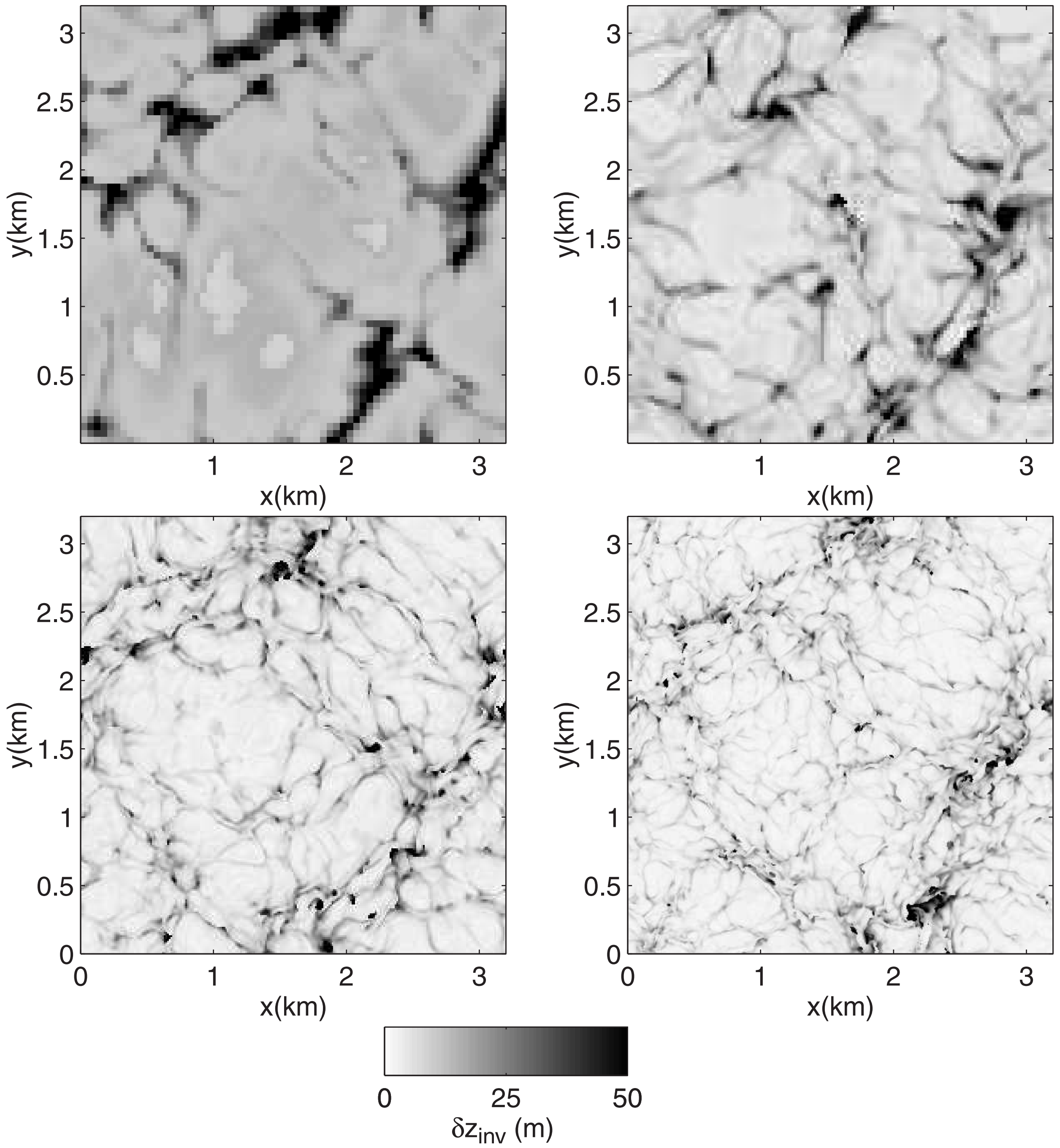

Figure 7:

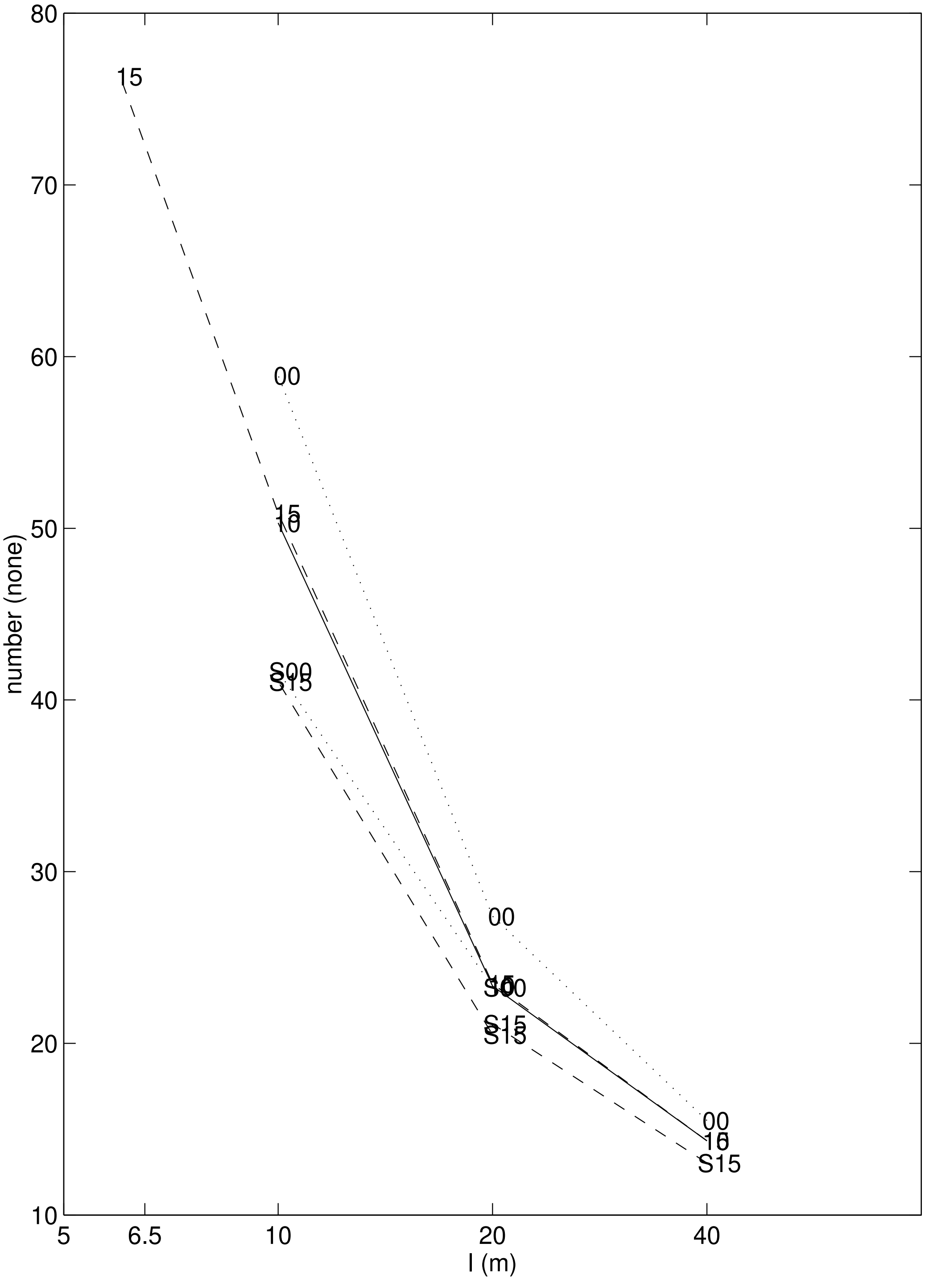

80
70
60
50
40
30
20
10
5
6.5
10
20
40
number (none)
l (m)
15
00
15
10
S00
S15
00
15
S0
S00
S15
S15
00
10
15
S15

Figure 8:

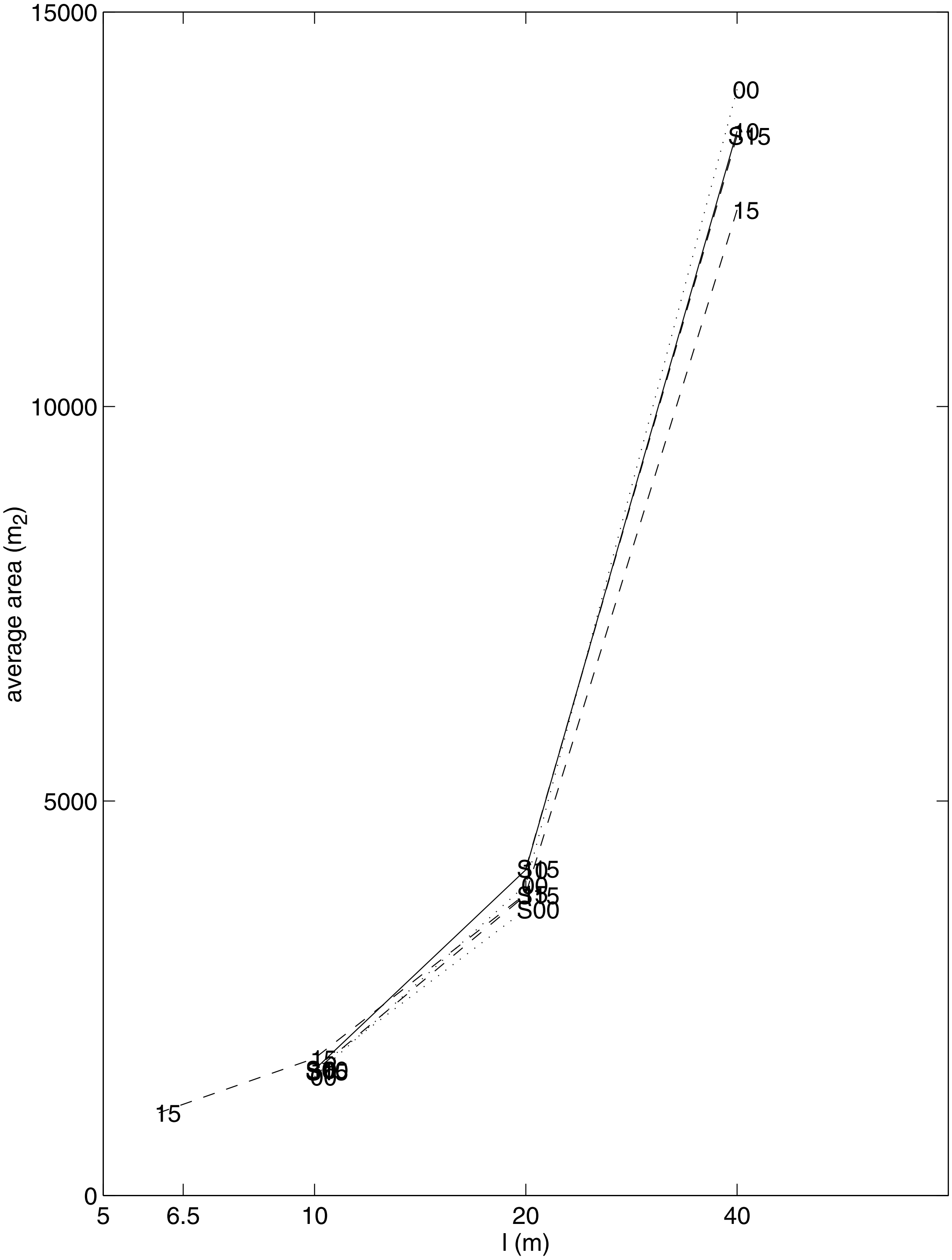

15000
10000
5000
0
average area (m2)
5
6.5
10
20
40
l (m)
00
10
S15
15
S15
00
S15
S00
15
S00
00
15

Figure 9:

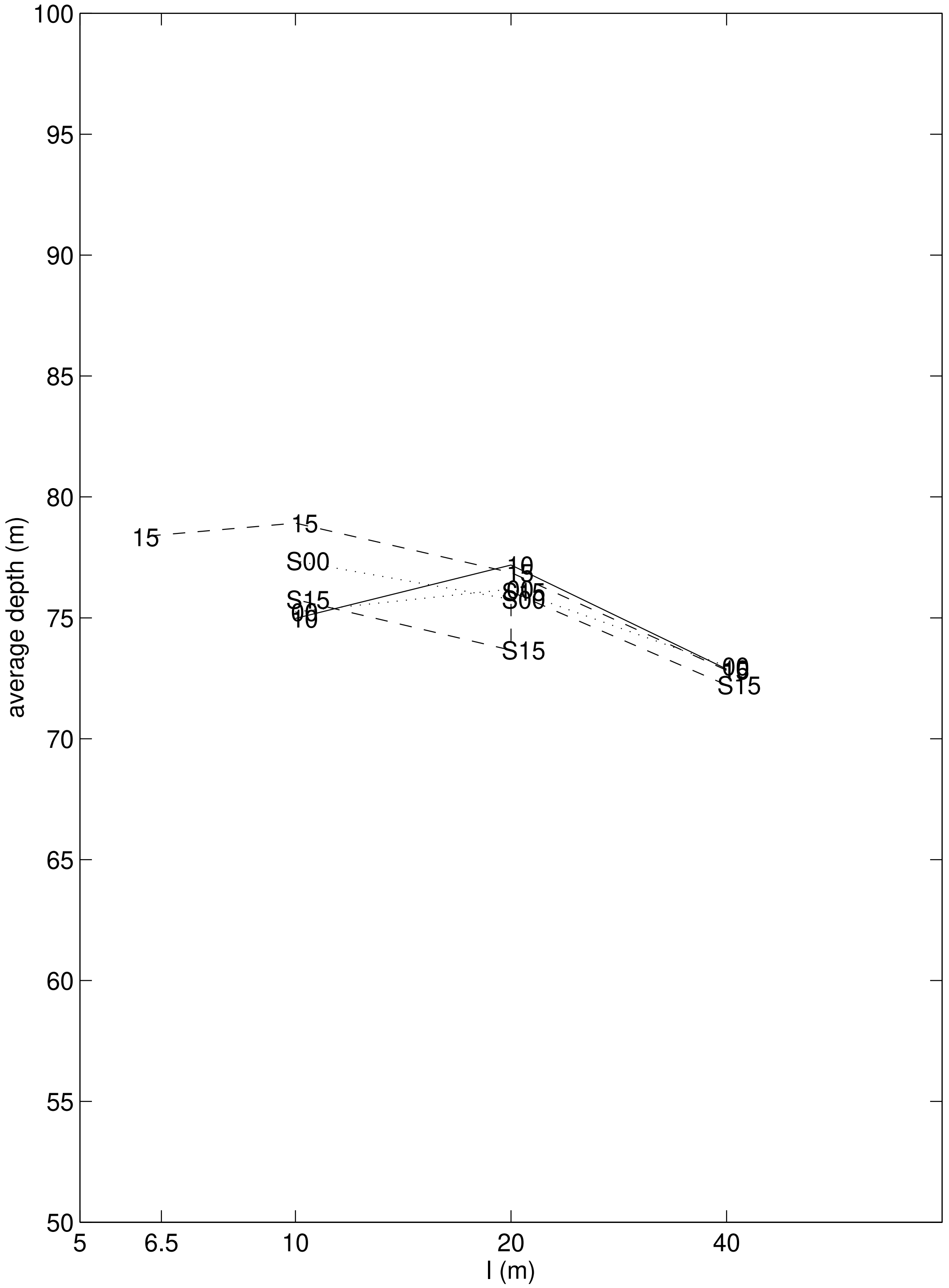

100
95
90
85
80
75
70
65
60
55
50
5
6.5
10
20
40
average depth (m)
l (m)
15
15
S00
S15
10
S15
S00
S15

Figure 10:

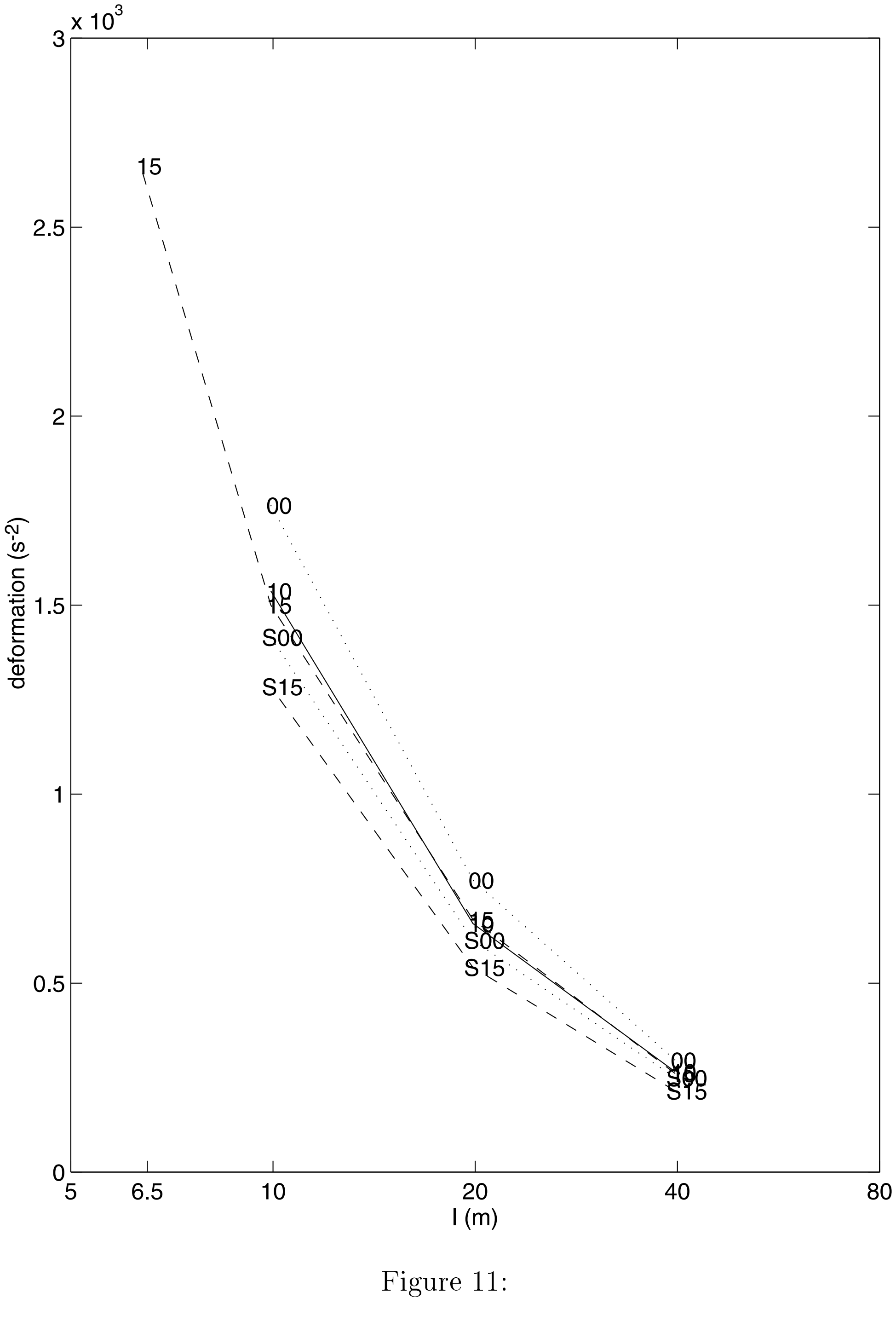

x 10^3
deformation (s^-2)
l (m)
0
0.5
1
1.5
2
2.5
3
5
6.5
10
20
40
80
15
00
10
15
S00
S15
00
15
S00
S15
00
S00
S15

Figure 11:

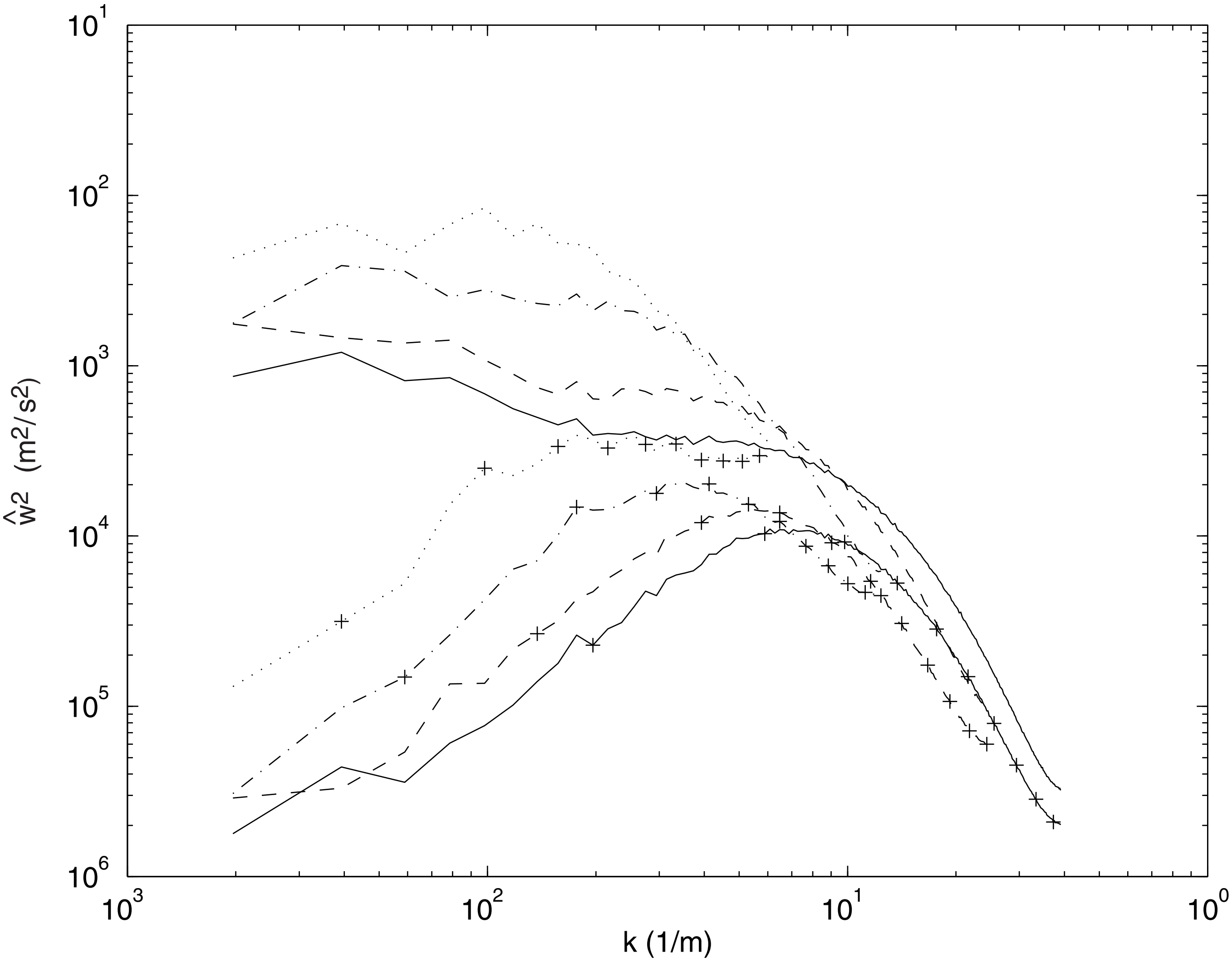

Figure 12:

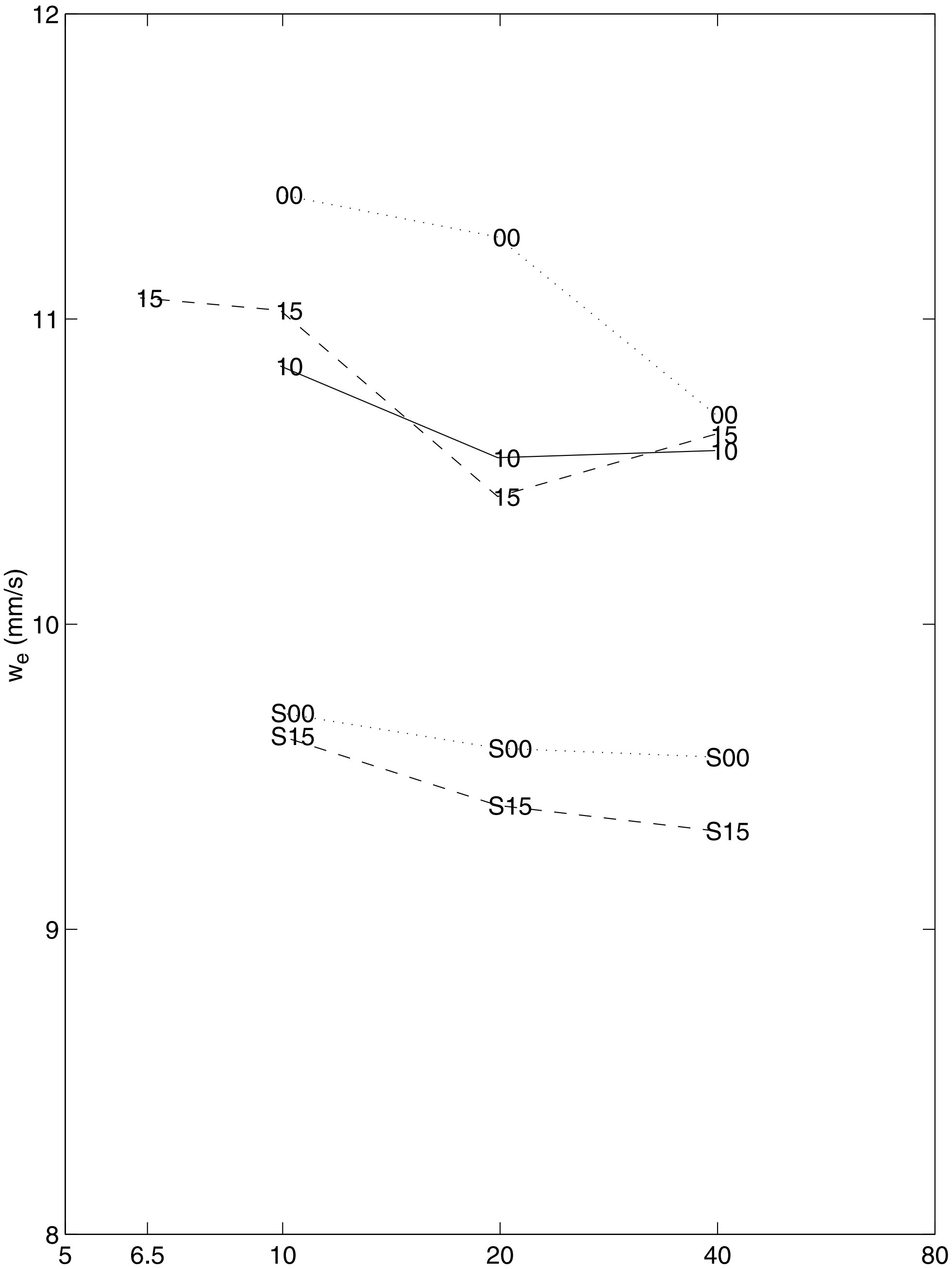
12
11
10
9
8
5
6.5
10
20
40
80
l (m)
w_e (mm/s)
00
00
00
15
15
15
15
10
10
10
S00
S00
S00
S15
S15
S15

Figure 13:

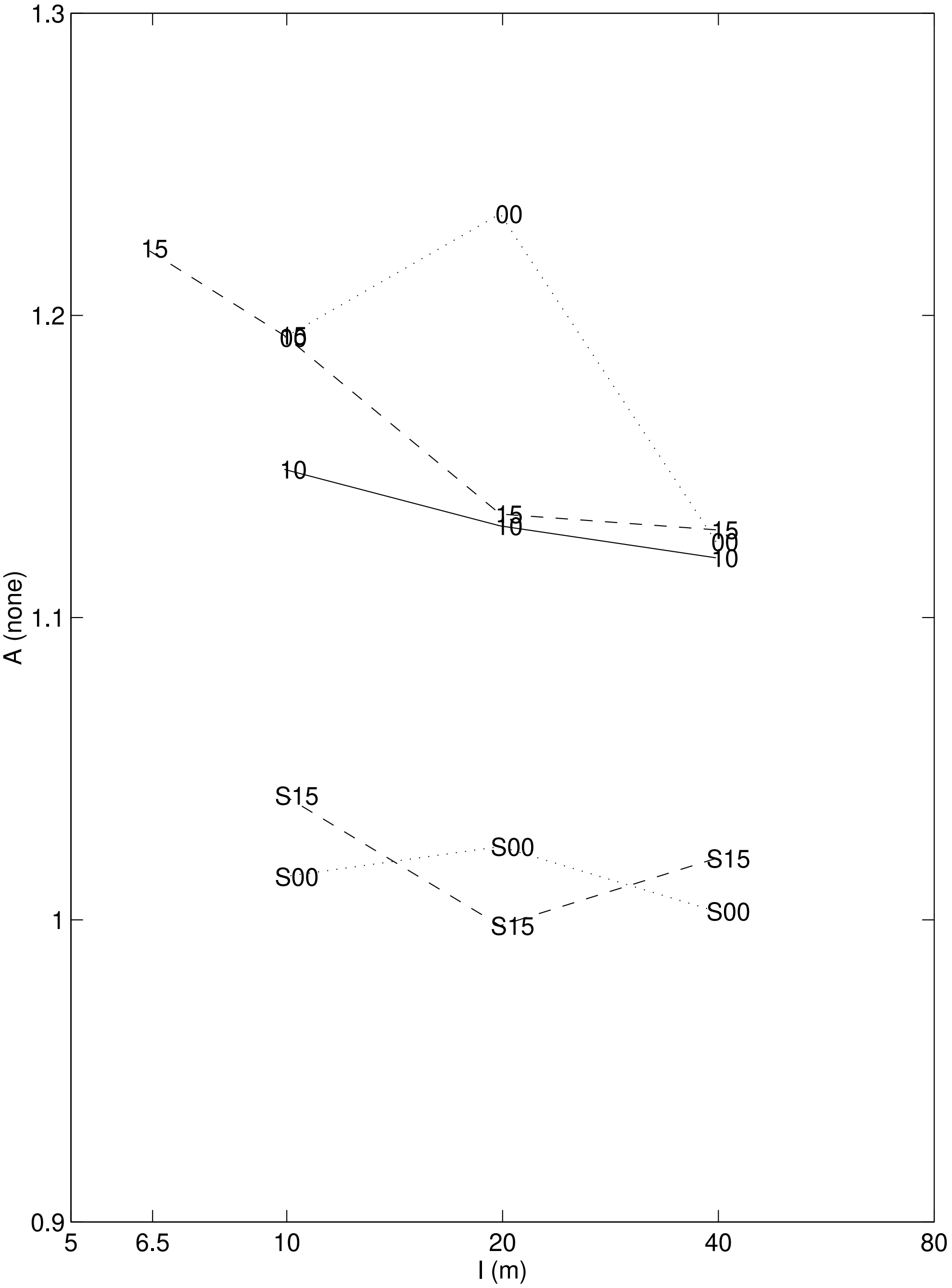

Figure 14:

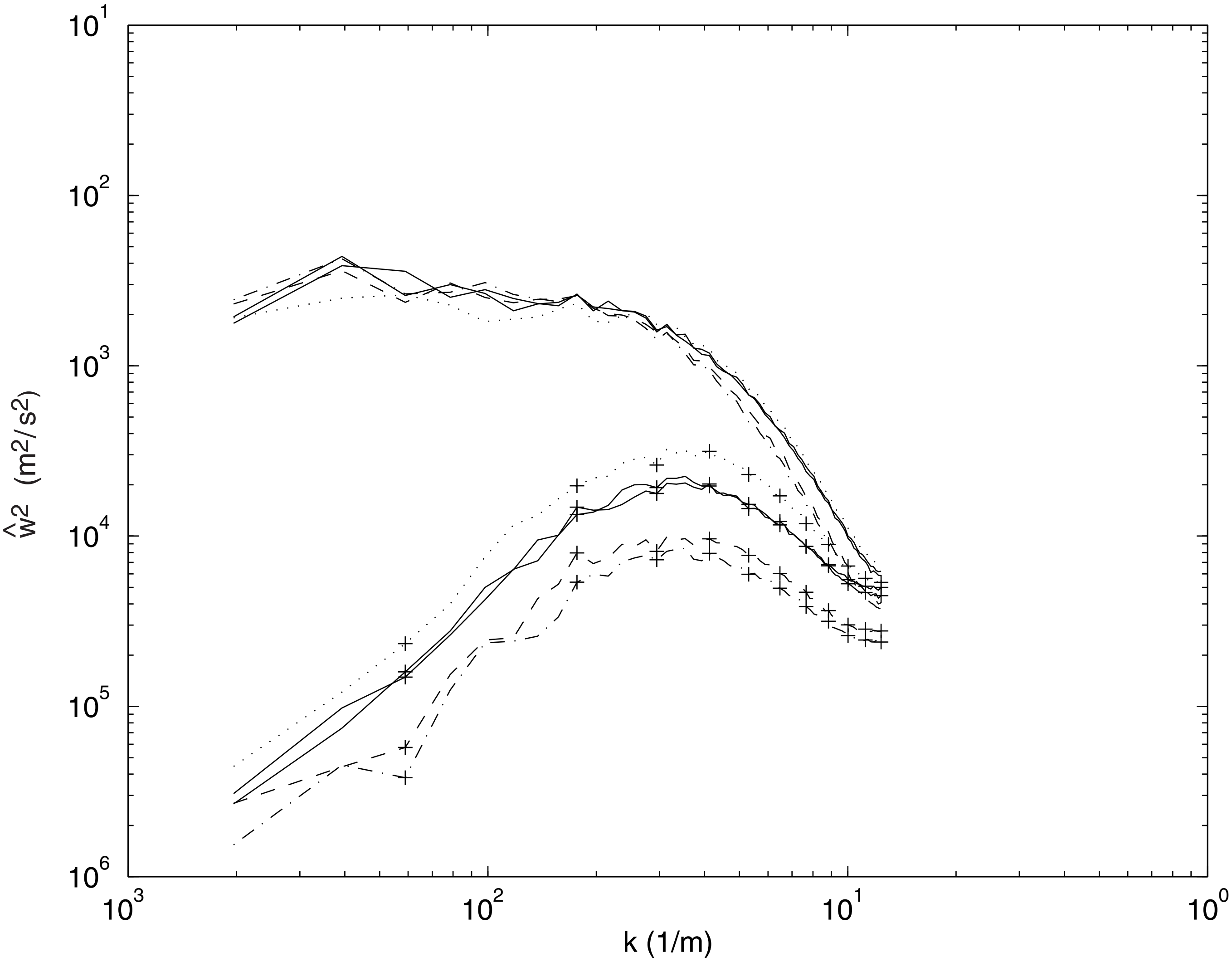

Figure 15: